Strain-insensitive micro torsion and temperature sensor based on a helical taper seven-core fiber structure

JUNNENG GUAN, SHUJIE XU, SHIYU LIU, GUITIAN QIU, ZHONGCHAO WEI, D CHUNHUA TAN, FAQIANG WANG, AND HONGYUN MENG* (D)

Guangdong Provincial Key Laboratory of Nanophotonic Function Materials and Devices, School of Information and Optoelectronic Science and Engineering, South China Normal University, Guangzhou 510006, China

*hymeng@scnu.edu.cn

Abstract: We propose a multimode interference-based optical fiber NHTSN sensor with a helical taper for simultaneous measurement of micro torsion and temperature. The sensor consists of single mode fiber (SMF), no-core fiber (NCF), and seven-core fiber (SCF). A helical taper is fabricated in the SCF using a flame heater, forming the SMF-NCF-Helical Taper SCF-NCF-SMF (NHTSN) structure. Theoretical analysis and experimental results demonstrate that the introduction of helical taper not only imparts directionality to the torsion measurement, but also results in a significant improvement in torsion sensitivity due to the increased inter-mode optical path difference (OPD) and enhanced inter-mode coupling. In the experiment, the torsion sensitivity of the NHTSN sensor reaches -1.255 nm/(rad/m) in the twist rate (TR) range of -3.931 rad/m to 3.931 rad/m, which is a 9-fold improvement over the original structure. Further reduction of the helical taper diameter increases the sensitivity to -1.690 nm/(rad/m). In addition, the sensor has a temperature sensitivity of up to 97 pm/°C from 20 °C to 90 °C, and simultaneous measurement of torsion and temperature is attainable through a dual-parameter measurement matrix. The NHTSN sensor possesses advantages of compact size, high sensitivity, good linearity, and strain-independence, endowing it with potential applications in structural health monitoring (SHM) and engineering machinery.

© 2024 Optica Publishing Group under the terms of the Optica Open Access Publishing Agreement

1. Introduction

Optical fiber sensors (OFSs) have emerged as pivotal technologies in the realm of sensing, owing to their notable advantages, including high sensitivity, compact structure, and strong anti-electromagnetic interference ability [1]. Applications of OFSs span diverse fields such as industry, agriculture, medicine, and biology, involving various external parameters, including temperature [2], deformation [3], refractive index (RI) [4], gas concentration [5], etc.

Structural health monitoring (SHM) of constructions like bridges, tunnels, and buildings is crucial. OFSs have gained attention in recent years for SHM due to their superior performances compared to conventional sensors, and they are now applied in measuring various deformation parameters such as strain [6], torsion [7], curvature [8], and transverse loading [9]. Torsion, a significant quantity in SHM, reflects the stress zone and internal state of structures [10]. Up to present, various optical fiber torsion sensors (OFTSs) based on different principles and structures have been proposed and fabricated. Early OFTSs predominantly measured torsion magnitude only, lacking the ability to determine torsion direction due to the absence of techniques to break the circular symmetry structure of optical fibers [11,12]. However, simultaneous measurement of both magnitude and direction is essential in most torsion monitoring applications.

To attain the ability for discriminating torsion direction, numerous effective methods have been proposed by researchers to introduce non-circular symmetry into the sensing area of OFTSs. Generally, there are two main methods to establish asymmetry in optical fibers. The first method is employing asymmetric specialty optical fibers as the sensing section such as polarization-maintaining fiber (PMF) [13], multicore fiber (MCF) [14], and photonic crystal fiber (PCF) [15]. The second method to realize the asymmetry involves introducing periodic refractive index modulation in the fibers through micro-machining, which can be divided into two ways. The first way is fabricating conventional long-period fiber gratings (LPFGs) or fiber Bragg gratings (FBGs) on the single mode fiber (SMF) by CO₂ laser irradiation [16–19], femtosecond laser micromachining [20,21], and so on. Another way is physical deformation, utilizing heat sources such as CO2 lasers, flame heaters, and arc discharges to heat and soften the fibers. External forces are then applied to fabricate shapes like helical and tapered structures. These two structures and their combination can effectively introduce asymmetric refractive index modulation in the fibers, enabling OFTSs to measure the torsion direction. Until now, based on physical deformation, numerous novel torsion sensors with excellent performance have been reported, including helical long-period fiber gratings (HLPFGs) [22-26], helical fiber Bragg gratings (HFBGs) [27,28], helical structures [29,30], tapered structures [31,32], and helical taper [33–37]. For instance, Zhao et al. proposed and demonstrated an improved HLPFG based on a SMF using a hydrogen-oxygen flame, in which the torsion sensitivity was significantly enhanced by adjusting the grating diameter and pitch [26]. Liu et al. realized a directional torsion sensor based on a HFBG fabricated on a triangular four-core fiber (TFCF). The helical TFCF was made by CO₂ laser irradiation while FBGs were written in the cores of the helical structure through defocusing phase mask method [28]. Zhang et al. reported a Mach-Zehnder interferometer (MZI) based sensor with a short helical structure formed in a MCF, capable of achieving simultaneous measurements of directional torsion and temperature [29]. Tan et al. proposed and fabricated a torsion sensor based on inter-core mode coupling in a tapered seven-core fiber (SCF). The discrimination of torsion direction and tunability of torsion sensitivity were achieved by introducing proper pre-twisting angles [31]. Zhu et al. manufactured a helical taper in a panda polarization-maintaining fiber through performing twist and pull simultaneously on the fiber with the assist of arc discharge, and the formed sensor exhibited a capability to measure both torsion magnitude and direction with a low temperature sensitivity [34]. The novel sensors mentioned above have been proven to be effective in improving the performance of torsion measurement, but some of them still suffer from several drawbacks, for instance, the relatively low torsion sensitivity prevents the sensor from recognizing micro torsion, the cross-sensitivity of strain or temperature reduces the accuracy of torsion measurement, and the complex fabrication process. Therefore, the research and development of highly sensitive torsion sensors capable of solving strain and temperature problems is the primary objective of OFTSs.

In this paper, a multimode interference-based optical fiber NHTSN sensor capable of simultaneously measuring micro torsion and temperature is proposed and fabricated. The sensor is assembled by splicing SMF, no-core fiber (NCF), and SCF, and utilizes a flame heater to create a helical taper in the SCF. From a theoretical perspective, it is inferred that the mechanism for improving torsion sensitivity with a helical taper involves increasing the inter-mode OPD and enhancing the inter-mode coupling, which is demonstrated through numerical simulation. The experimental results indicate that the addition of helical taper enhances the torsion sensitivity by a factor of 9, increasing from -0.138 nm/(rad/m) to -1.255 nm/(rad/m) within the range of -3.931 rad/m to 3.931 rad/m, while also realizing the identification of torsion direction. The sensitivity is increased to -1.690 nm/(rad/m) after further reducing the diameter of helical taper. Additionally, the NHTSH sensor exhibits a response to external temperature (20 °C to 90 °C) measured to be 97 pm/°C and demonstrates insensitivity to strain variation. Finally, the

simultaneous measurement of micro torsion and temperature can be achieved by deriving a dual-parameter measurement matrix.

2. Sensor structure and working principle

2.1. Sensor structure

The schematic diagram of the proposed NHTSN sensor is illustrated in Fig. 1(a). The sensor structure consists of a section of SCF with a helical taper, two pieces of NCFs, as well as lead-in and lead-out SMFs. The cross-section image of the SCF (MC1010-A, YOFC, China) is shown in Fig. 1(b). It contains seven Ge-doped cores surrounded by seven trenches and one cladding, one of which is located in the center of the fiber, and the other six cores are evenly distributed around it in a regular hexagonal shape. The center core and six outer cores have the same diameter of 8 μ m and the distance between two adjacent cores is 41.5 μ m. Each trench has a first and second layer with diameters of 18 μ m and 30 μ m, respectively, and the diameter of the cladding is 150 μ m. In addition, the core/cladding diameters of NCF and SMF we used are 0 /125 μ m and 9 /125 μ m, respectively.

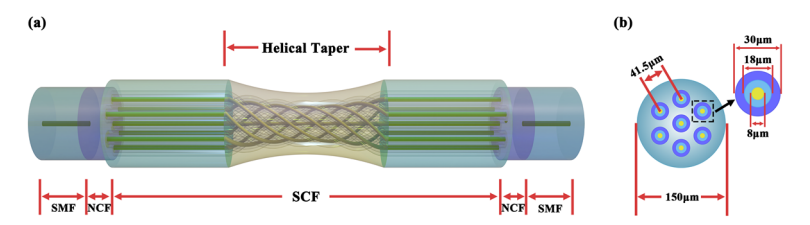


Fig. 1. (a) Schematic diagram of the NHTSN sensor. (b) Cross-section image of SCF.

2.2. Working principle

For the proposed sensor, when the transmitted light from the lead-in SMF reaches the first NCF, multiple modes are excited due to the mode field mismatch and subsequently coupled into the SCF. Due to the geometry and RI distribution of SCF, only three modes are able to propagate stably, center core mode (CCM), outer core mode (OCM), and cladding mode (CM). The middle part of the SCF is twisted and stretched simultaneously by flame heater to form a helical taper. For the helical structure, the outer cores and cladding are twisted into helical shapes, while the center core remains almost straight. Therefore, the effective optical path lengths and effective RIs of OCM and CM are increased, while those of CCM remain unchanged. For the taper structure, the core distance becomes smaller, which strengthen the crosstalk among the cores, and thus enhances the coupling between CCM and OCM. The combination of the above two structures has excellent effects in introducing the optical path difference (OPD) and enhancing the inter-mode coupling. Subsequently, a series of interferences among CCM, OCM and CM occur at the second NCF, and finally the light is recoupled back into the lead-out SMF. In the following, we present a theoretical analysis of the helical region and taper region of the helical taper, respectively.

As mentioned above, the helical region plays an important role in changing the effective refractive index and optical path length. According to the multimode interference theory, the light intensity generated by N different mode components can be expressed as [29]:

$$I = \sum_{i=1}^{N} I_i + 2 \sum_{i=1}^{N} \sum_{j=2}^{N} \sqrt{I_i I_j} \cos(\Delta \varphi_{ij}),$$
 (1)

where I_i and I_j are the light intensities of the guided modes, and the subscripts i and j represent the orders of the modes (i and j are integers, i < j). $\Delta \varphi_{ij}$ denotes the phase difference between the

i-th mode and *j*-th mode, which can be written as the following equation:

$$\Delta \varphi_{ij} = \varphi_i - \varphi_j = \frac{2\pi \Delta n_{eff}^{ij} L}{\lambda},\tag{2}$$

where Δnij eff = (ni eff - nj eff) represent the effective RI difference between mode i and j. Lis the physical propagation length, and λ is the wavelength of the incident light. According to Eq. (1), when $\Delta \varphi_{ij} = (2 m + 1) \pi$, $m = 0, \pm 1, \pm 2...$, the condition of destructive interference is satisfied, resulting in a minimum of light intensity. The wavelength corresponding to the resonant dips in the transmission spectrum can be derived as:

$$\lambda = \frac{2\Delta n_{eff}^{ij} L}{2m+1}. (3)$$

Considering several features of the proposed NHTSN interferometer, such as the helical taper structure, a series of Mach-Zehnder interferences between any two modes among CCM, OCM and one dominant CM, and the sufficiently short NCFs without accumulation of phase differences between modes. Based on these features, further derivation is applied to Eq. (3), and the interference dips wavelengths of the NHTSN structure can be obtained:

$$\lambda_{12} = \frac{2[(n_{eff}^{1,H}L_H - n_{eff}^{2,H}L_H^{oc}) + (n_{eff}^{1,S} - n_{eff}^{2,S})L_S]}{2m+1},\tag{4}$$

$$\lambda_{13} = \frac{2[(n_{eff}^{1,H} - n_{eff}^{3,H})L_H + (n_{eff}^{1,S} - n_{eff}^{3,S})L_S]}{2m+1},$$

$$\lambda_{23} = \frac{2[(n_{eff}^{2,H}L_H^{oc} - n_{eff}^{3,H}L_H) + (n_{eff}^{2,S} - n_{eff}^{3,S})L_S]}{2m+1},$$
(5)

$$\lambda_{23} = \frac{2[(n_{eff}^{2,H}L_H^{oc} - n_{eff}^{3,H}L_H) + (n_{eff}^{2,S} - n_{eff}^{3,S})L_S]}{2m+1},$$
(6)

where λ_{12} , λ_{13} and λ_{23} represent the resonant dips wavelengths of the interferences between CCM and OCM, CCM and CM, as well as OCM and CM, respectively. n1,H eff(n1,S eff), n2,H eff(n2,S eff) and n3,H eff(n3,S eff) denote the effective RIs of CCM, OCM and CM propagating in the helical region (straight region) of the SCF, respectively. L_H , L_S and $Loc\ H$ are the physical propagation lengths of the helical region, straight region and helical outer cores, correspondingly.

For the taper region of SCF, it serves to enhance the coupling effects among the seven cores, which can be approximated as enhancing the coupling between CCM and OCM. According to the mode coupling theory, the linear interaction and propagation of M arbitrary modes in the single-mode waveguides can be expressed as [38]:

$$i\frac{d}{dz}A = \overline{C_M}A,\tag{7}$$

where the elements of vector A denote the complex amplitude of the electric field along the z direction for each core. C_M represent the coupling matrix explaining the interaction between any two of the M cores, which can be derived as:

$$\overline{C_M} = \begin{pmatrix}
\beta_0 & c_{01} & c_{02} & \dots & c_{0(M-1)} \\
c_{10} & \beta_1 & c_{12} & \dots & c_{1(M-1)} \\
c_{20} & c_{21} & \beta_2 & \dots & c_{2(M-1)} \\
\vdots & \vdots & \vdots & \ddots & \vdots \\
c_{(M-1)0} & c_{(M-1)1} & c_{(M-1)2} & \dots & \beta_{(M-1)}
\end{pmatrix}, (8)$$

where β_i is the propagation constant of the fundamental mode in the i-th core and c_{ii} is the coupling coefficient between the i-th and j-th cores. In general, the mode propagation constants

in independent waveguides are different, i.e., $\beta_i \neq \beta_j$, and modes interact in pairs under certain conditions, i.e., $c_{ij} \neq 0$. The coupling matrix $\overline{C_M}$ completely describes the pairwise interactions of the M cores and well reduces the modeling of arbitrary coupled systems to the solution of the matrix elements. Based on the premise of the weakly guided approximation, utilizing the principle of light wave interaction between two parallel single-mode waveguides, the coupling coefficient c of two almost identical circular cores can be written as [39,40]:

$$c = \frac{\sqrt{2\Delta}}{r} \frac{U^2}{V^3} \frac{K_0(Wd/r)}{K_1^2(W)},\tag{9}$$

where $\Delta = (n2\ co-n2\ cl)/2n2\ co$ represent the relative RI difference between the core and cladding of SCF. r and d are the core radius and center distance between two adjacent cores of the taper SCF, respectively. The modified Hankel functions of order 0 and 1 are denoted by K_0 and K_1 , respectively. V, U and W are the normalized frequency, and the normalized transverse propagation constants of the LP $_{01}$ mode in the fiber core and cladding, respectively, which can be defined as:

$$V = rk_0 \sqrt{n_{co}^2 - n_{cl}^2}, \ U = r\sqrt{k_0^2 n_{co}^2 - \beta^2}, \ W = (V^2 - U^2)^{1/2}, \tag{10}$$

where $k_0 = 2\pi/\lambda_0$ denotes the wave number corresponding to the wavelength λ_0 in vacuum. β is the propagation constant of each core in the absence of inter-core mode coupling. Equations (9) and (10) reveal that the coupling coefficient c depends primarily on the core radius r and the adjacent cores distance d. Therefore, tapering the SCF inevitably leads to changes in the coupling strength and mode field distribution.

The above are the basic principles of helical region and taper region. When external torsion is applied to the sensor, the fiber RI changes due to the photo-elastic effect, which can be written as $n_{\tau} = n_0(1 + \rho^2 \tau^2)^{1/2} \approx n_0(1 + \rho^2 \tau^2/2)$ [41,42], where n_0 is the initial RI without twisting, ρ is the radial distance between the torsion point and the center of the fiber, and $\tau = \pi \theta/180^{\circ}L$ is the twist rate (TR), where θ and L are the angle and length of the torsion, respectively. For the proposed helical taper, there is a permanent initial TR τ_0 before the torsion τ is applied, so the fiber RI changes based on formula nHT $\tau \approx n_0[1 + \rho^2(\tau \pm \tau_0)^2/2]$, where " \pm " indicates two different torsion directions, the same as the pre-twist direction is defined as clockwise (CW) direction (+) and the opposite is defined as counter clockwise (CCW) direction (-). The RI change of the center core is negligible because the ρ of center core is much smaller than that of the outer cores and cladding [43]. Therefore, with the variation of the applied torsion, the effective RIs of the OCM and CM change, while that of the CCM remains unchanged. According to Eqs. (4)-(6), the wavelength shifts caused by TR variation $\Delta \tau$ can be derived as:

$$\Delta \lambda_{12} \approx \frac{2}{2m+1} \left[\frac{\partial n_{eff}^{1,H}}{\partial \tau} L_H - \frac{\partial n_{eff}^{2,H}}{\partial \tau} L_H^{oc} + \frac{\partial (n_{eff}^{1,S} - n_{eff}^{2,S})}{\partial \tau} L_S \right] \Delta \tau, \tag{11}$$

$$\Delta \lambda_{13} \approx \frac{2}{2m+1} \left[\frac{\partial (n_{eff}^{1,H} - n_{eff}^{3,H})}{\partial \tau} L_H + \frac{\partial (n_{eff}^{1,S} - n_{eff}^{3,S})}{\partial \tau} L_S \right] \Delta \tau, \tag{12}$$

$$\Delta \lambda_{23} \approx \frac{2}{2m+1} \left[\frac{\partial n_{eff}^{2,H}}{\partial \tau} L_H^{oc} - \frac{\partial n_{eff}^{3,H}}{\partial \tau} L_H + \frac{\partial (n_{eff}^{2,S} - n_{eff}^{3,S})}{\partial \tau} L_S \right] \Delta \tau, \tag{13}$$

where $\Delta\lambda_{12}$, $\Delta\lambda_{13}$ and $\Delta\lambda_{23}$ represent the torsion-induced wavelength shifts of the resonant dips generated by the interferences between CCM and OCM, CCM and CM, as well as OCM and CM, respectively. Since it is micro torsion, the length variation of the fiber can be neglected according to the material mechanics theory [44], so there is no need to perform partial differential operation on the length.

When the ambient temperature changes, both the mode effective RIs and fiber length vary due to the thermo-optic effect and thermal expansion effect. For silica, the thermo-optic coefficient is far greater than the thermal expansion coefficient [45]. Therefore, only the mode effective RIs need to be partially differentiated while the length variation of the fiber is negligible. In fiber, the effective thermo-optic coefficient can be written as $\xi_{eff} = dn_{eff}/n_{eff}dT$, where n_{eff} and T denote effective RI and ambient temperature, respectively. Considering the structural characteristics of the NHTSN sensor, the following equations can be obtained:

$$\delta(n_{eff}^{i,k} - n_{eff}^{j,k}) = (\xi_k^{co} n_{eff}^{i,k} - \xi_k^{cl} n_{eff}^{j,k}) \Delta T, \tag{14}$$

where δ is the variable of $(ni, k \ eff - nj, k \ eff)$, $ni, k \ eff$ and $nj, k \ eff$ represent the mode effective RIs $(i \ and \ j \ are integers, \ 1 \le i < j \le 3, \ k \ is both \ H \ or \ S)$. $\xi co \ k \ and \ \xi cl \ k$ denote the thermo-optic coefficients of cores and cladding, respectively. Similarly, the wavelength shifts caused by temperature variation ΔT can be obtained by substituting Eq. (14) into Eqs. (11)-(13) and changing τ to T. The temperature sensitivity mainly depends on the relationship between $\xi co \ k$ and $\xi cl \ k$ [46]. When $\xi co \ k$ is greater than $\xi cl \ k$, the sensitivity is positive, the resonant dip will shift towards longer wavelength. For the SCF we used, since $\xi co \ k$ is greater than $\xi cl \ k$, the resonant dip will theoretically shift towards longer wavelength with increasing temperature.

2.3. Numerical simulation

The working principle is verified by numerical simulation using COMSOL Multiphysics 5.6. Modal field distribution of SCF is simulated by finite element method (FEM) according to actual physical parameters. As shown in Figs. 2(a)-(c), CCM, OCM and dominant CM are displayed respectively, and they have different effective RIs. It can be seen from the figures that the effective mode areas of these three modes are relatively small without tapering operation, which indicates that the coupling strength between modes is at a weak level. According to the above theoretical analysis, coupling coefficient depends on core radius and adjacent cores distance. Therefore, tapering the SCF is a feasible method to enhance inter-mode coupling. Figures 2(d)-(f) show the modal field distribution of SCF with a taper waist diameter of $105\,\mu m$. The effective mode areas of CCM, OCM and dominant CM increase significantly, which proves that the increase of coupling coefficient can promote the mode interaction and power coupling.

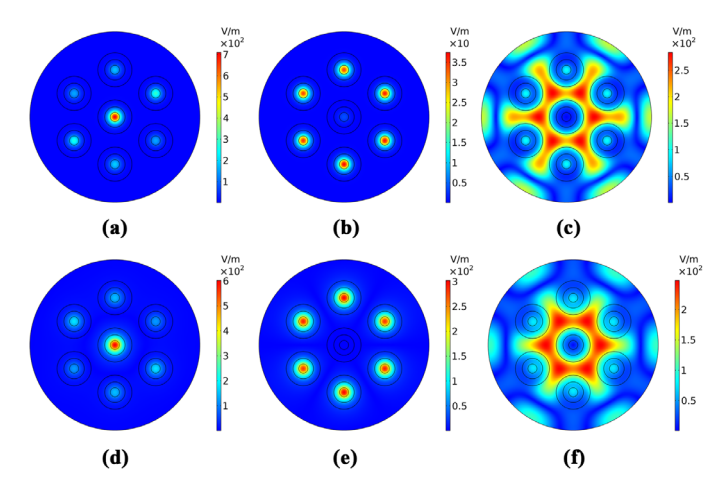


Fig. 2. Modal field distribution of the original SCF includes (a) CCM, (b) OCM, (c) dominant CM, and that of the $105\,\mu m$ tapered SCF includes (d) CCM, (e) OCM, (f) dominant CM.

3. Sensor fabrication process

The fabrication process of the NHTSN sensor is divided into three steps, as shown in Fig. 3(a). Step 1, a SMF and a section of NCF were coaxially spliced together by a fusion splicer, and the NCF was then cleaved to 2 mm with a high precision optical fiber cleaver. The reason for choosing a length of 2 mm for NCF is that experiments have demonstrated that it can fulfill the function of an optical coupler without introducing excessive OPD. Another same configuration was prepared by repeating the step above. They are defined as lead-in SMF-NCF (LIS-N) and lead-out SMF-NCF (LOS-N), respectively. Step 2, a 33 mm SCF was sandwiched between LIS-N and LOS-N. Step 3, the cascaded structure obtained above was fixed by the rotator stage and fiber clamp, with BBS and OSA connected at each end to observe spectral changes and select high-quality spectra during tapering. A pre-twist angle was applied, and then the flame heater was activated to preheat the middle portion of SCF with a low power flame to make it malleable. Subsequently, increased the flame power and move the two three-axis displacement platforms outward at the same speed. The distance moved directly determines the parameters of helical taper. After that, the helical taper was permanently introduced into the SCF, forming the LIS-N-Helical Taper SCF-N-LOS structure, referred to as NHTSN.

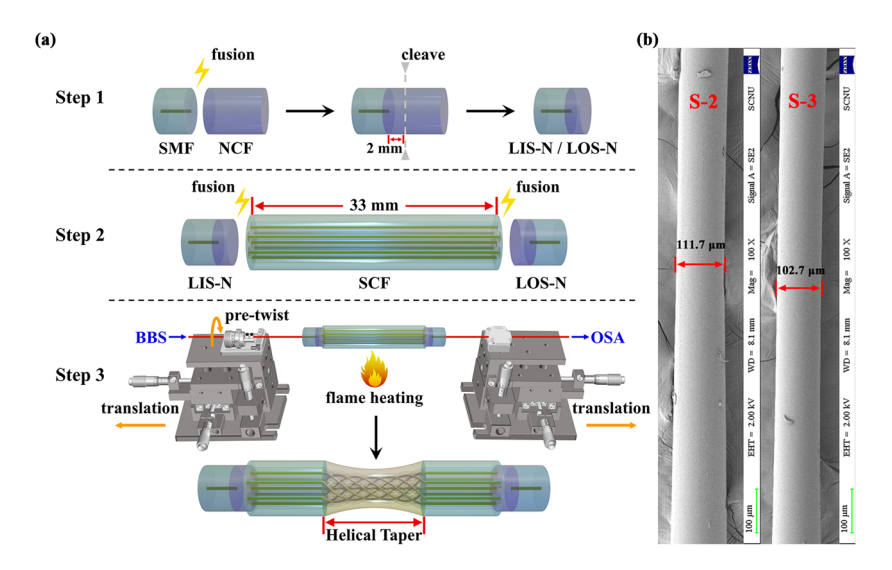


Fig. 3. (a) Fabrication process of the NHTSN sensor. (b) SEM images of S-2 and S-3.

Figure 4(a) displays the transmission spectrum of the NHTSH sensor. The maximum extinction ratio (ER) is about 12.54 dB and the free spectral range (FSR) is about 17.74 nm. To further theoretically analyze the mode characteristics, a fast Fourier transform (FFT) is performed and the obtained spatial frequency spectrum is shown in Fig. 4(b). The dominant peak at 0 nm⁻¹, the secondary peak at 0.19 nm⁻¹ and the third peak at 0.59 nm⁻¹ represent CCM, OCM and dominant CM, respectively. The FFT result demonstrates the excitation of CCM, OCM and CM and their participation in the interferences. The amplitude distribution indicates that the interferences are mainly contributed by CCM and OCM, while the contribution of CM is relatively small. Combined with the numerical simulation results, we can summarize the advantages of using SCF for interferenceters. The formed core-core modes interference is more stable compared to ordinary core-cladding modes interference. Moreover, since SCF has six outer cores, according to mode coupling theory in the principle section, its OCM has higher optical power than OCM of MCF with fewer cores (e.g., three-core optical fiber).

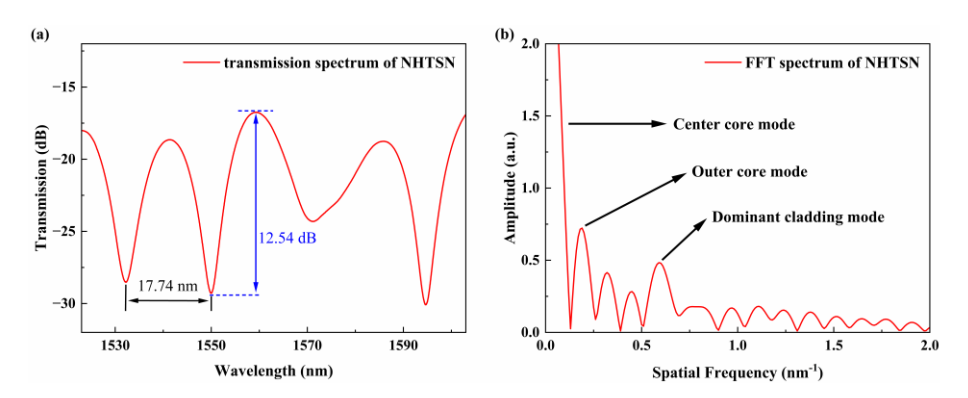


Fig. 4. (a)Transmission spectrum of the HNTSN sensor. (b) FFT of the transmission spectrum.

4. Experiment results and discussion

4.1. Torsion response characteristics

The schematic diagram of the experimental device for testing the torsion characteristics of NHTSN sensor is shown in Fig. 5. Both ends of the sensor are stably fixed on the rotator stage and fiber clamp of two three-axis displacement platforms respectively. By slightly adjusting the translation stage, the fiber is left in its natural straightened state, and the distance between two fixation points is measured as ~11.1 cm. The torsional loading distance includes the sensor length and a portion of SMF. This is because in practical experimental operations, it is necessary to reserve 1-2 cm of bare SMF for cutting and fusion splicing. At the same time, to avoid damaging the fiber, the positions of the two fiber clamps are set at the plastic jacket of SMF instead of the bare fiber. This is based on the premise that we have experimentally verified that the torsional response of SMF is almost zero and the torsion sensitivities are almost the same for different loading distances. The input end of the sensor is connected to a broadband source (BBS), and the output end is connected to an optical spectrum analyzer (OSA) for spectrum measurement. During the torsion experiment, the rotator was rotated 25° in CW direction and CCW direction with a step of 5°. Correspondingly, the sensor was progressively applied twist rate from 0 to 3.931 rad/m and 0 to -3.931 ram/m in CW and CCW directions in steps of 0.786 rad/m.

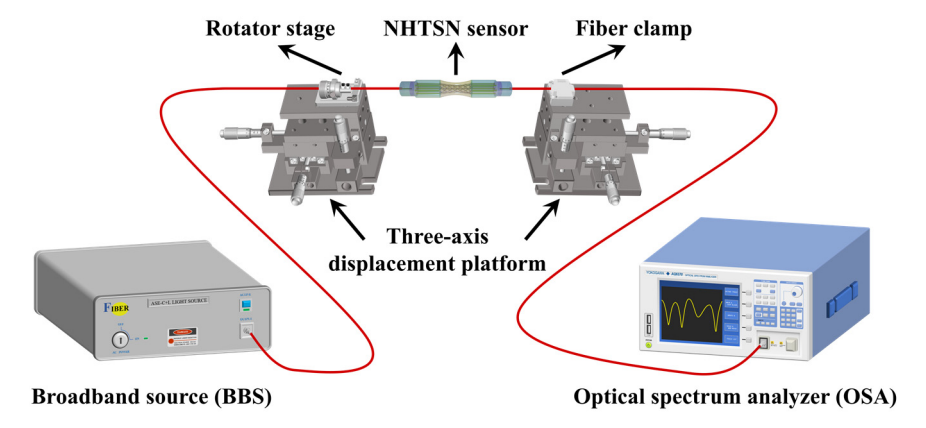


Fig. 5. Schematic diagram of the experimental device for torsion (strain) characteristics testing.

To investigate the relationship between helical taper and torsion sensitivity, three samples were prepared for the experiment: sample 1 (S-1) without any treatment, sample 2 (S-2, waist diameter $\approx 111.7\,\mu m)$ and sample 3 (S-3, waist diameter $\approx 102.7\,\mu m)$ with the same pre-twist angle but different waist diameters, and the SEM images are shown in Fig. 3(b). Firstly, the torsion response of S-1 was measured. The interference spectra with different twist rates are shown in Fig. 6, where (a) and (b) correspond to CW and CCW directions, respectively. As can be seen, with the increase of TR, there are only slight variations in wavelength and intensity of the resonant dips, illustrating that the torsion sensitivity of SCF sensor without helical taper is very low (-0.138 nm/(rad/m)). This is because the inter-mode OPD and inter-core coupling coefficient are small. The weak interference and coupling effects are insufficient to make spectrum responsive to external disturbances.

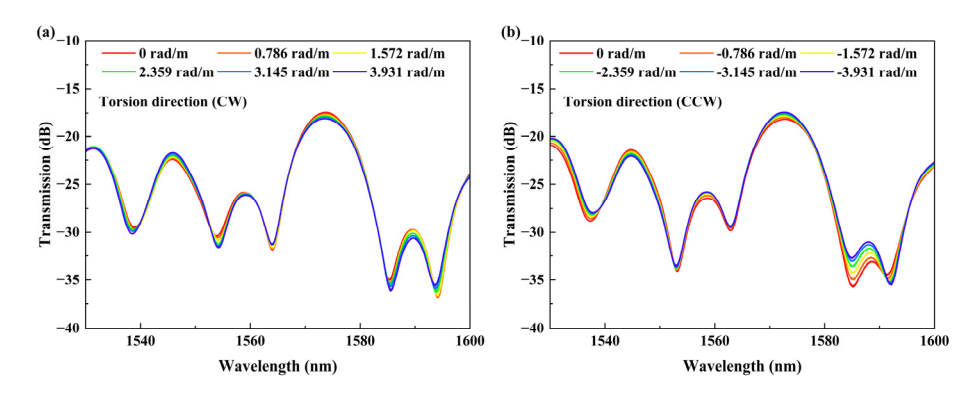


Fig. 6. Interference spectra of S-1 sensor at different twist rates in (a) CW direction and (b) CCW direction.

Secondly, to experimentally verify the improvement of torsion sensitivity by introducing the helical taper, the same torsion experiment was performed on S-2. The results are displayed in Fig. 7, where (a) and (b) refer to the responses of interference spectrum varying with different twist rates in CW direction and CCW direction, respectively, and (c) represent the corresponding wavelength shift data and linear fitting. As seen in the spectrum, the four distinct resonant dips (Dip A-D) shift towards shorter (longer) wavelength when the sensor is twisted from 0 rad/m to 3.931 rad/m (-3.931 rad/m) with an increment of 0.786 rad/m in CW (CCW) direction. The correlation between resonant wavelength of Dip A-D and twist rate is presented in Fig. 7(b), where the torsion sensitivities are -1.255 nm/(rad/m), -1.198 nm/(rad/m), -0.935 nm/(rad/m), and -1.139 nm/(rad/m) with R-squared (coefficient of determination) of about 0.996, 0.996, 0.994, and 0.993, respectively. Compared with S-1, there is a significant improvement in torsion sensitivity, reaching 9 times. Moreover, the torsion resolution of the sensor is calculated as 1.59×10^{-2} rad/m based on the scanning accuracy of OSA.

From the comparison of experimental results of S-1 and S-2, it is clear that the helical taper structure has a remarkable effect on the improvement of torsion sensitivity, attributed to the following two points. First, the outer cores and cladding are pre-twisted into helical shape while the center core remains straight, so the length of physical propagation path and refractive index increase, leading to an increase in optical paths of OCM and CM. When external torsion is exerted on the sensor, the resultant shear stress significantly influences the optical paths of OCM and CM, while having minimal impact on that of CCM. Therefore, the OPDs between modes vary greatly, leading to a high sensitivity to torsion. Second, the tapering operation reduces the physical dimensions of SCF, including the core and cladding diameters, as well as the core distance, which promotes the power coupling among CCM, OCM and CM. The strong coupling effect renders the modal field more susceptible to the external environment, hence, the torsion sensitivity of the

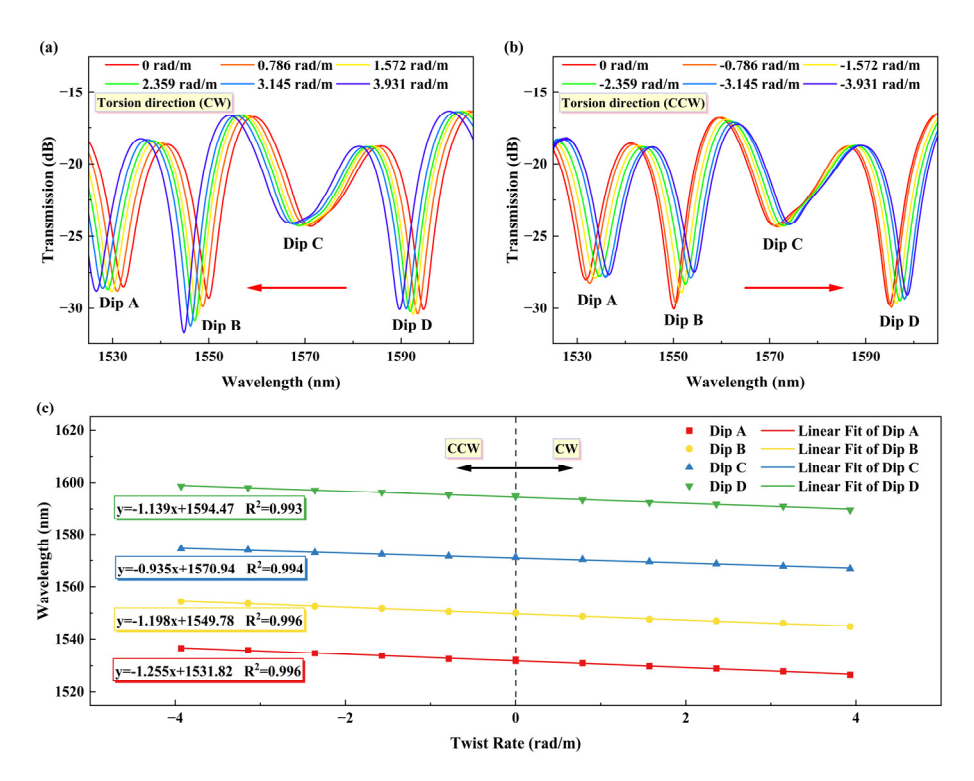


Fig. 7. Interference spectra of S-2 sensor at different twist rates in (a) CW direction and (b) CCW direction. (c) Wavelength shift data and linear fitting of resonant dips A-D.

sensor is significantly enhanced. Furthermore, the four resonant dips exhibit varying levels of torsion sensitivity, which can be interpreted as the inclusion of a series of interferences in the transmitted light signal, as mentioned in the theoretical section. For multimode interference, the sensitivities corresponding to different resonant dips are generally different, due to the fact that each dip represents a specific mode interference [47]. Finally, during both CW and CCW torsion, Dip A-D display opposite shift directions in wavelength as TR increases. This can be explained by the relationship between OPD and torsion direction. Since the CW direction aligns with the pre-twist direction, OPD decreases with the increase of TR. According to equations (11) to (13), this results in a blue shift in resonant wavelength. Following the same principle, the increase of OPD leads to a red shift in the CCW direction.

In order to explore the potential enhancement in torsion sensitivity through a reduction in waist diameter of the helical taper, we fabricated and tested S-3. The experimental results are displayed in Figs. 8(a)-(c). As evident from the spectrum, the wavelength response of the resonant dips to twist rate is consistent with S-2. Dip A and Dip B exhibit sensitivities of -1.690 nm/(rad/m) and -1.647 nm/(rad/m) with R-squared of 0.924 and 0.986, respectively, and the torsion resolution is 1.18 rad/m. In comparison with S-2, the maximum torsion sensitivity is improved from -1.255 nm/(rad/m) to -1.690 nm/(rad/m), reflecting an enhancement of ~34.66%. However, concurrently, three drawbacks are evident: a decline in spectral smoothness and regularity, a reduction in the number of sensitive dips, and a deterioration in fitting linearity. Reducing the waist diameter is a mixed blessing. On one hand, the strong inter-mode coupling effect enhances the light field's sensitivity to external disturbances, thus increasing the torsion sensitivity. On the other hand, it sacrifices the mechanical properties of the sensor to some extent, resulting in a decline in spectral performance. This decline is mainly manifested in the recovery

of the spectral initial state. Recovery experiments were performed on six NHTSN sensors with different waist diameters. Figure 9 illustrates the wavelength and transmission of the resonant dips when TR returns to 0 rad/m compared to the initial state. As the waist diameter decreases from $150\,\mu m$ to $71.6\,\mu m$, the average variables of wavelength are $1.26\,n m$, $0.21\,n m$, $1.93\,n m$, $0.72\,n m$, $0.92\,n m$, and $1.81\,n m$, respectively, as shown in Fig. 9(a), while the average variable of transmission are $1.53\,d B$, $0.61\,d B$, $6.6175\,d B$, $3.45\,d B$, $4.81\,d B$, and $5.34\,d B$, respectively, as shown in Fig. 9(b). It can be seen that as the waist diameter decreases, the wavelength recovery remains good, while transmission recovery gradually deteriorates. Therefore, when designing the helical taper diameter, it is necessary to comprehensively consider spectral quality, measurement recoverability, sensor sensitivity and fiber mechanical strength.

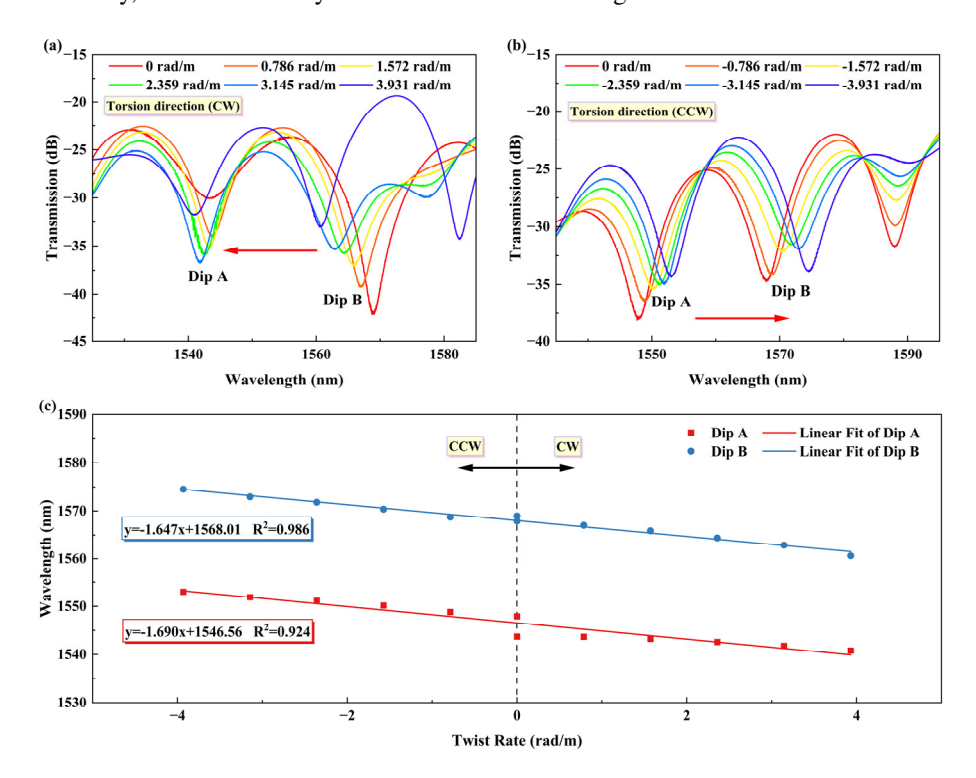


Fig. 8. Interference spectra of S-3 sensor at different twist rates in (a) CW direction and (b) CCW direction. (c) Wavelength shift data and linear fitting of resonant dips A and B.

Generally, an optical fiber sensor is not only sensitive to an individual external physical quantity. To ensure the accuracy of measurement results, it is imperative to take cross-sensitivity into consideration. Hence, experiments were conducted to assess the sensor's responsiveness to both temperature and strain. S-2 was selected as the experimental group due to its superior comprehensive performance, while S-1 was chosen as the control group to analyze the influence of helical taper.

4.2. Temperature response characteristics

The experimental setup for temperature response measurement is shown in Fig. 10. A BBS, OSA, and a constant temperature and humidity chamber (CTHC) were employed. Throughout the experiment, the sensor was positioned within the enclosed CTHC. The temperature was incrementally raised from 20 °C to 90 °C in 10 °C intervals, while maintaining the relative

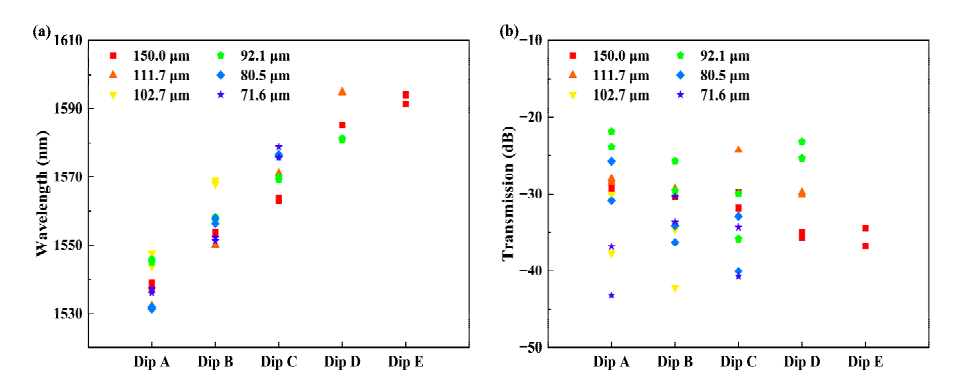


Fig. 9. (a) Wavelength and (b) transmission recovery of NHTSN sensors with different waist diameters.

humidity at ambient levels (80%). Each temperature level was sustained for around 10 minutes to ensure stability, and the transmission spectra were recorded with OSA.



Fig. 10. Schematic diagram of the experimental device for temperature characteristics testing.

The experimental results of S-1 are displayed in Fig. 11. The spectrum response in Fig. 11(a) reveals that the resonant dips shift toward longer wavelength as the temperature increases. Figure 11(b) illustrates the linear relationship between wavelengths of the three dips and temperature variation. As can be seen, the respective temperature sensitivities of Dip A-C are measured to be 70 pm/°C, 46 pm/°C, and 44 pm/°C with R-squared of 0.985, 0.971, 0.986, respectively.

The same experiment was conducted on S-2, with the corresponding results presented in Fig. 12. Similarly, the spectral response exhibits a red shift, and the temperature sensitivities of Dip A-D are measured to be 69 pm/°C, 70 pm/°C, 97 pm/°C, and 54 pm/°C, with R-squared of 0.996, 0.995, 0.966, 0.996, respectively. The temperature resolution is calculated to be 0.21 °C. In addition, as the temperature increases, the resonant dips of S-1 and S-2 both shift towards longer wavelength, which is consistent with the theoretical analysis.

Upon comparing the experimental results of S-1 and S-2, the introduction of helical taper enhances the maximum temperature sensitivity from 70 pm/°C to 97 pm/°C, representing an improvement of about 38.6%. It follows that the rise in temperature sensitivity is less pronounced compared to torsion sensitivity (9 times). The heightened sensitivity corroborates the role of the OPD introduced by helical taper. The disparity in amplification stems from distinct mechanisms. In accordance with the thermo-optic effect, alterations in temperature induce the same trend

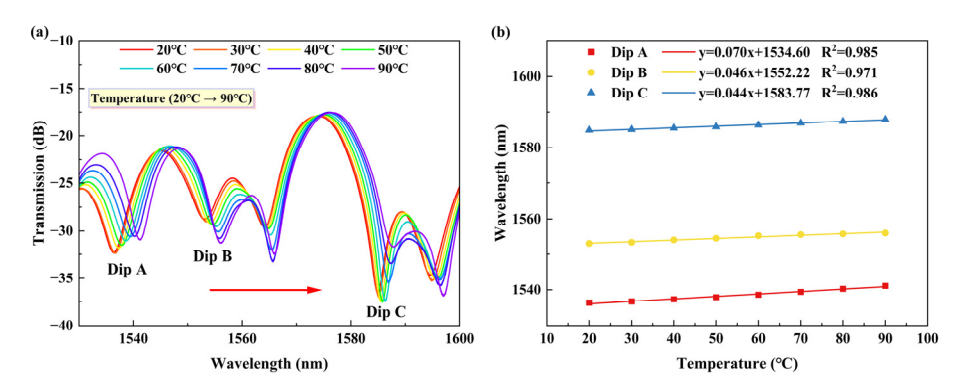


Fig. 11. (a) Interference spectra of S-1 sensor at different temperatures. (b) Wavelength shift data and linear fitting of resonant dips A-C.

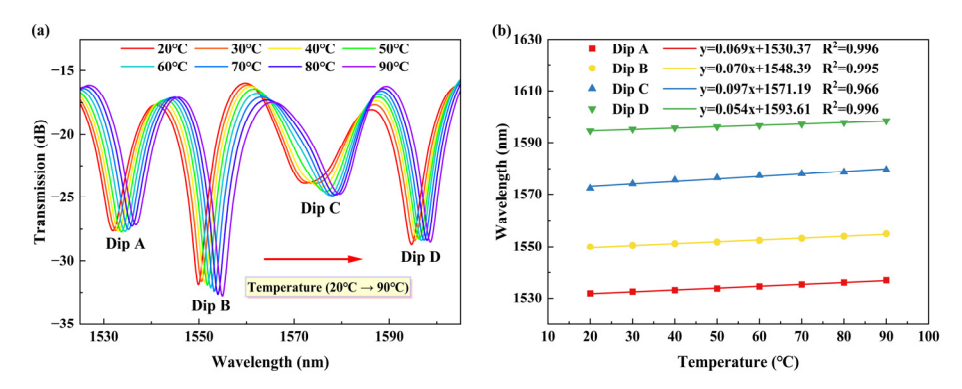


Fig. 12. (a) Interference spectra of S-2 sensor at different temperatures. (b) Wavelength shift data and linear fitting of resonant dips A-D.

change in RIs of cores and cladding. Meanwhile, the photo-elastic effect dictates that variations in TR cause different degrees of changes in RIs of outer cores and cladding. Therefore, the change rates of OPD vary between the two cases, resulting in different sensitivity increments.

4.3. Strain response characteristics

The strain response was tested with the experimental device in Fig. 5. In the strain experiment, the rotator stage remained stationary, while the axial strain on the sensor was increased from 0 μ E to 1750 μ E by manipulating the translation stage. From the results in Fig. 13, the maximum strain sensitivities of S-1 and S-2 are measured to be -0.54 pm/ μ E and 1.02 pm/ μ E, respectively, with a difference of 88.9%, demonstrating the positive effect of helical taper. It is noteworthy that the strain-torsion crosstalk of S-2 is calculated to be -8.13 \times 10⁻⁴ (rad/m)/ μ E, which is negligible. Hence, it can be approximated that there is no impact of strain variation on torsion response.

In order to make the conclusions rigorous, three additional NHTSN sensors with smaller cone waist diameters were fabricated to explore whether the strain sensitivity increases with the decrease of the conical diameter. The measurement results are shown in Fig. 14, where the maximum strain sensitivities of the sensors with conical diameters of 92.1 μ m, 80.5 μ m, and 71.6 μ m are -0.28 pm/ μ e, -0.34 pm/ μ e, and 0.88 pm/ μ e, respectively. From this, we can approximately assume that the proposed NHTSN sensor is strain-insensitive.

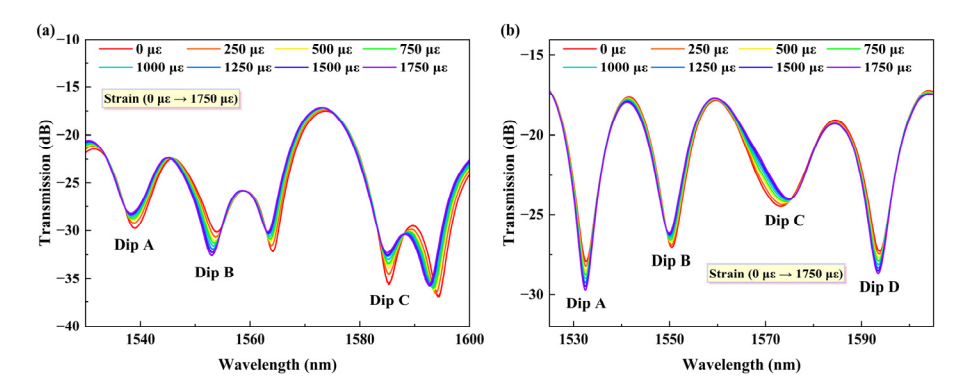


Fig. 13. Interference spectra of (a) S-1 sensor and (b) S-2 sensor at different strains.

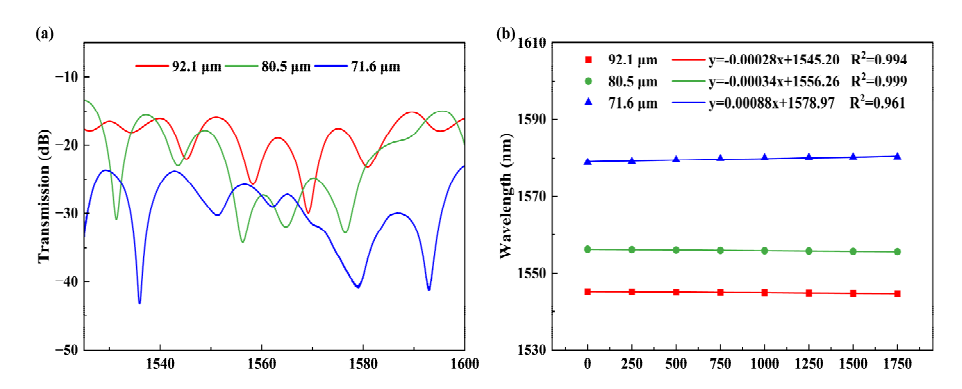


Fig. 14. (a) Interference spectra of NHTSH sensors with different conical diameters. (b) Wavelength shift data and linear fitting.

4.4. Measurement repeatability of torsion and temperature

Repeatability is an important indicator for evaluating the performance of the NHTSN sensor. After placing the S-2 sensor for 7 days, the torsion and temperature responses were retested using the above method under the same external conditions. The results of the first and second experiments are displayed in Fig. 15. For torsion measurement, the maximum error rates for repeatability of Dip A-D are 0.087%, 0.084%, 0.078%, and 0.091%, respectively. For temperature measurement, the maximum error rates for repeatability of Dip A-D are 0.061%, 0.068%, 0.076%, and 0.092%, respectively. It can be seen that the proposed sensor has excellent measurement repeatability.

4.5. Simultaneous measurement of torsion and temperature

The above experimental results indicate that the NHTSN sensor (S-2) is sensitive to both torsion and temperature. Therefore, a dual-parameter measurement matrix is derived to achieve simultaneous measurement of torsion and temperature, as follows:

$$\begin{pmatrix} \Delta \tau \\ \Delta T \end{pmatrix} = \begin{pmatrix} A_{\tau} & A_{T} \\ B_{\tau} & B_{T} \end{pmatrix}^{-1} \begin{pmatrix} \Delta \lambda_{A} \\ \Delta \lambda_{B} \end{pmatrix} = \frac{1}{A_{\tau}B_{T} - A_{T}B_{\tau}} \begin{pmatrix} B_{T} & -A_{T} \\ -B_{\tau} & A_{\tau} \end{pmatrix} \begin{pmatrix} \Delta \lambda_{A} \\ \Delta \lambda_{B} \end{pmatrix}, \quad (15)$$

where $\Delta \tau$, ΔT , $\Delta \lambda_A$ and $\Delta \lambda_B$ represent the torsion and temperature variations, wavelength changes of Dip A and Dip B, respectively. The torsion and temperature sensitivities of Dip A (Dip B) are

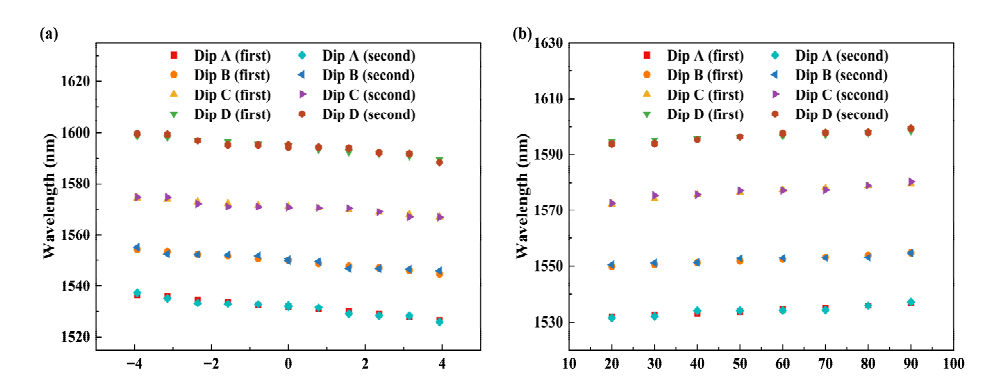


Fig. 15. Results of repeatability experiments on (a) torsion and (b) temperature.

denoted by A_{τ} and A_{T} (B_{τ} and B_{T}), respectively. By substituting the experimental results into Eq. (15), the following equations can be obtained:

$$\begin{pmatrix} \Delta \tau \\ \Delta T \end{pmatrix} = \frac{1}{-5188} \begin{pmatrix} 70 & -69 \\ 1198 & -1255 \end{pmatrix} \begin{pmatrix} \Delta \lambda_A \\ \Delta \lambda_B \end{pmatrix}. \tag{16}$$

When external torsion and temperature vary, the interference dips Dip A and Dip B respond and undergo wavelength shifts. By substituting the wavelength changes into Eq. (16), both torsion and temperature variations can be obtained simultaneously. The condition number of the dual-parameter measurement matrix is calculated as 481.6592 [48]. This evaluation method calculates a loose estimate of the maximum error bound. Based on this, we performed further error analysis to quantify the errors in $\Delta \tau$ and ΔT due to inaccurate determination of $\Delta \lambda_A$ and $\Delta \lambda_B$. In this case, the maximum measurement error can be written as [49]:

$$|\delta \Delta \tau| \le \frac{|B_T||\delta \Delta \lambda_A| + |A_T||\delta \Delta \lambda_B|}{|A_\tau B_T - A_T B_\tau|} = \frac{70|\delta \Delta \lambda_A| + 69|\delta \Delta \lambda_B|}{5188},\tag{17}$$

$$|\delta\Delta T| \le \frac{|B_{\tau}||\delta\Delta\lambda_A| + |A_{\tau}||\delta\Delta\lambda_B|}{|A_{\tau}B_T - A_TB_{\tau}|} = \frac{1198|\delta\Delta\lambda_A| + 1255|\delta\Delta\lambda_B|}{5188},\tag{18}$$

where $\delta \Delta \tau$, $\delta \Delta T$, $\delta \Delta \lambda_A$, $\delta \Delta \lambda_B$ represent the errors in $\Delta \tau$, ΔT , $\Delta \lambda_A$, $\Delta \lambda_B$, respectively. It can be concluded that the errors in $\Delta \lambda_A$ and $\Delta \lambda_B$ are transferred to $\Delta \tau$ and ΔT . The corresponding transfer coefficients are determined by the matrix characteristics and are independent of $\Delta \tau$ and ΔT . The optimization of matrix characteristics can be achieved through numerical stability techniques or the introduction of preconditioned matrix.

The sensitivity matrix was experimentally validated to evaluate the feasibility and error rate during the simultaneous measurement of torsion and temperature. The rotator stage and fiber clamp were placed in the CTHC and the S-2 sensor was fixed inside. At the beginning, the TR and temperature were set to -1.396 rad/m and 25 °C, respectively. After stabilization, the TR and temperature were varied to 2.094 rad/m and 55 °C, with variations of 3.49 rad/m and 30 °C, respectively. The spectral response of the sensor is displayed in Fig. 16. It can be obtained that $\Delta \lambda_A$ and $\Delta \lambda_B$ are -2.30 nm and -2.08 nm, respectively. Substitute $\Delta \lambda_A$ and $\Delta \lambda_B$ into Eq. (16), and the calculation results of $\Delta \tau$ and ΔT are 3.3693 rad/m and 27.9491 °C, respectively. The error rates between experimental value and calculated value for torsion and temperature are 0.1207 rad/m and 2.0509 °C, with relative errors of 3.46% and 6.84%, respectively. Therefore, in cases where the relative errors are less than 10% [9], it can be approximated that the NHTSN sensor has the ability to measure torsion and temperature simultaneously.

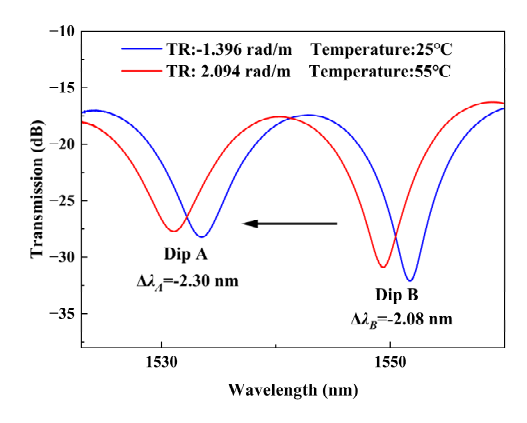


Fig. 16. Spectra response of S-2 sensor at different twist rates and temperatures.

Table 1 shows the comparison between the NHTSN sensor proposed in this paper and other representative torsion sensors. Our work has relatively high sensitivity in micro torsion sensing and has certain advantages in simultaneous measurement of torsion and temperature. However, there are some limitations, such as the relatively small measurement range and inferior torsion sensitivity compared to TSC-HLPGs [25] and Helical Taper PMF [34].

Table 1. Performance comparison of optical fiber torsion sensors with different fabrication methods and structures

Method	Fabrication	Structure	Torsion Sensitivity	Range	Temperature Sensitivity	Reference
Asymmetric fiber	/	PMF-SI	43 pm/°	-300° to 300°	1	[13]
	/	Spun-MCF	0.23 pm/°	-270° to 270°	/	[14]
	/	LFTPCF	0.466 nm/(rad/m)	-57 to 57 rad/m	/	[15]
Periodic refractive index modulation	CO ₂ laser	R-LPFGs	0.084 nm/(rad/m)	-100 to 100 rad/m	20 pm/°C	[19]
	Femtosecond laser	LPFG	0.182 nm/(rad/m)	-105 to 105 rad/m	/	[21]
	CO2 laser	TSC-HLPGs	3.54 nm/(rad/m)	-360° to 360°	58.8 pm/°C	[25]
	Arc discharge	HFBG	0.065 nm/(rad/m)	-75 to 75 rad/m	60.51 pm/°C	[27]
	Oxyhydrogen flame	SFTPCF	0.208 nm(rad/m)	-76 to 76 rad/m	/	[30]
	CO ₂ laser	Taper MCF	0.12-1.00 nm/°	160°-940°	/	[31]
	Arc discharge	Helical Taper PMF	-3.191 nm/(rad/m)	-13.57 to 13.57 rad/m	9 pm/°C	[34]
	Oxyhydrogen flame	Helical Taper DSHF	-1.67 nm/(rad/m)	-5.627 to 5.627 rad/m	7.66 pm/°C	[36]
	Flame heater	Helical Taper MCF	-1.690 nm/(rad/m)	-3.931 to 3.931 rad/m	97 pm/°C	This paper

5. Conclusion

In summary, the NHTSN sensor with a helical taper based on multimode interference has been experimentally demonstrated to be able to simultaneously measure directional micro torsion and external temperature without strain cross-sensitivity. Theoretical analysis and experimental results both indicate that introducing a helical taper into the SCF can effectively enhance torsion

and temperature sensitivity. Within the TR range of $-3.931 \, \text{rad/m}$ to $3.931 \, \text{rad/m}$, the torsion sensitivity of the NHTSN sensor is measured to be $-1.255 \, \text{nm/(rad/m)}$ (a 9-fold increase). In the range of 20 °C to 90 °C, the temperature sensitivity is 97 pm/°C (a 38.6% increase). There is a certain degree of improvement in torsion sensitivity with the decrease in helical taper diameter, reaching $1.690 \, \text{nm/(rad/m)}$. Featured with compact size, high sensitivity, and good linearity, the NHTSN sensor is well-suited for applications in structural health monitoring and engineering machinery.

Funding. Science and Technology Planning Project of Guangzhou, China (202201011590); National Natural Science Foundation of China (11674109, 61774062); Science and Technology Planning Project of Guangdong Province (2017A020219007).

Disclosures. The authors declare no conflicts of interest.

Data Availability. Data underlying the results presented in this paper are not publicly available at this time but may be obtained from the authors upon reasonable request.

References

- 1. K. T. V. Grattan and T. Sun, "Fiber optic sensor technology: an overview," Sens. Actuators, A 82(1-3), 40-61 (2000).
- C. X. Yue, H. Ding, W. Ding, et al., "Weakly-coupled multicore optical fiber taper-based high-temperature sensor," Sens. Actuators, A 280, 139–144 (2018).
- C. Ma, D. H. Wang, J. Wang, et al., "A compact sensor capable of temperature, strain, torsion and curvature measuring," J. Lightwave Technol. 40(14), 4896–4902 (2022).
- Z. D. Zhu, D. X. Ba, L. Liu, et al., "Temperature-compensated distributed refractive index sensor based on an etched multi-core fiber in optical frequency domain reflectometry," Opt. Lett. 46(17), 4308–4311 (2021).
- N. Bavili, T. Balkan, B. Morova, et al., "Highly sensitive optical sensor for hydrogen gas based on a polymer microcylinder ring resonator," Sens. Actuators, B 310, 127806 (2020).
- C. B. Zhang, T. G. Ning, J. J. Zheng, et al., "An optical fiber strain sensor by using of taper based TCF structure," Opt. Laser Technol. 120, 105687 (2019).
- 7. D. J. Liu, R. Kumar, F. F. Wei, *et al.*, "Highly sensitive twist sensor based on partially silver coated hollow core fiber structure," J. Lightwave Technol. **36**(17), 3672–3677 (2018).
- O. Arrizabalaga, Q. Sun, M. Beresna, et al., "High-performance vector bending and orientation distinguishing curvature sensor based on asymmetric coupled multi-core fibre," Sci. Rep. 10(1), 14058 (2020).
- Y. C. Li, Z. Song, J. P. Wei, et al., "Fiber in-line Mach-Zehnder interferometer for simultaneous measurement of transverse loading and temperature based on multi-core fiber," Opt. Laser Technol. 143, 107354 (2021).
- B. B. Song, Y. P. Miao, W. Lin, et al., "Multi-mode interferometer-based twist sensor with low temperature sensitivity employing square coreless fibers," Opt. Express 21(22), 26806–26811 (2013).
- 11. K. Itoh, T. Saitoh, and Y. Ohtsuka, "Optical rotating sensing by the geometric effect of fiber-loop twisting," J. Lightwave Technol. **5**(7), 916–919 (1987).
- S. Wei, W. Zhang, J. Shang, et al., "Torsion sensing characteristics of fibre ring laser based on nonlinear polarisation rotation," Electron. Lett. 48(2), 116–118 (2012).
- 13. X. J. Liu, F. J. Wang, J. R. Yang, *et al.*, "Fiber ring laser directional torsion sensor with ultra-wide linear response," Sensors 19(16), 3613 (2019).
- I. Floris, J. Madrigal, S. Sales, et al., "Twisting measurement and compensation of optical shape sensor based on spun multicore fiber," Mech. Syst. Signal Process 140, 106700 (2020).
- F. Zhang, Y. Wang, Z. Y. Bai, et al., "Helicity enhanced torsion sensor based on liquid filled twisted photonic crystal fibers," Sensors 20(5), 1490 (2020).
- Y. P. Wang and Y. J. Rao, "Long period fibre grating torsion sensor measuring twist rate and determining twist direction simultaneously," Electron. Lett. 40(3), 164–166 (2004).
- Y. P. Wang, J. P. Chen, and Y. J. Rao, "Torsion characteristics of long-period fiber gratings induced by high-frequency CO2 laser pulses," J. Opt. Soc. Am. B 22(6), 1167–1172 (2005).
- Y. J. Rao, T. Zhu, and Q. J. Mo, "Highly sensitive fiber-optic torsion sensor based on an ultra-long-period fiber grating," Opt. Commun. 266(1), 187–190 (2006).
- L. L. Shi, T. Zhu, Y. E. Fan, et al., "Torsion sensing with a fiber ring laser incorporating a pair of rotary long-period fiber gratings," Opt. Commun. 284(22), 5299–5302 (2011).
- B. Huang and X. W. Shu, "Ultra-compact strain- and temperature-insensitive torsion sensor based on a line-by-line inscribed phase-shifted FBG," Opt. Express 24(16), 17670–17679 (2016).
- X. R. Dong, Z. Xie, Y. X. Song, et al., "Highly sensitive torsion sensor based on long period fiber grating fabricated by femtosecond laser pulses," Opt. Laser Technol. 97, 248–253 (2017).
- L. L. Xian, P. Wang, and H. P. Li, "Power-interrogated and simultaneous measurement of temperature and torsion using paired helical long-period fiber gratings with opposite helicities," Opt. Express 22(17), 20260–20267 (2014).
- L. Zhang, Y. Q. Liu, X. B. Cao, et al., "High sensitivity chiral long-period grating sensors written in the twisted fiber," IEEE Sensors J. 16(11), 4253–4257 (2016).

- M. Deng, J. S. Xu, Z. Zhang, et al., "Long period fiber grating based on periodically screw-type distortions for torsion sensing," Opt. Express 25(13), 14308–14316 (2017).
- R. Subramanian, C. L. Zhu, H. Zhao, et al., "Torsion, strain, and temperature sensor based on helical long-period fiber gratings," IEEE Photon. Technol. Lett. 30(4), 327–330 (2018).
- 26. Y. Y. Zhao, S. Liu, J. X. Luo, *et al.*, "Torsion, refractive index, and temperature sensors based on an improved helical long period fiber grating," J. Lightwave Technol. **38**(8), 2504–2510 (2020).
- J. Li, G. Y. Chen, P. Ma, et al., "Sampled Bragg gratings formed in helically twisted fibers and their potential application for the simultaneous measurement of mechanical torsion and temperature," Opt. Express 26(10), 12903–12911 (2018)
- Y. Liu, A. Zhou, and L. B. Yuan, "Multifunctional fiber-optic sensor, based on helix structure and fiber Bragg gratings, for shape sensing," Opt. Laser Technol. 143, 107327 (2021).
- 29. H. L. Zhang, Z. F. Wu, P. P. Shum, *et al.*, "Directional torsion and temperature discrimination based on a multicore fiber with a helical structure," Opt. Express **26**(1), 544–551 (2018).
- 30. F. Zhang, S. Liu, Y. Wang, *et al.*, "Highly sensitive torsion sensor based on directional coupling in twisted photonic crystal fiber," Appl. Phys. Express **11**(4), 042501 (2018).
- F. Z. Tan, Z. Y. Liu, J. J. Tu, et al., "Torsion sensor based on inter-core mode coupling in seven-core fiber," Opt. Express 26(16), 19835–19844 (2018).
- 32. D. X. Sun, X. J. Liu, F. J. Wang, *et al.*, "Bias twisting in side-tapered PMF Sagnac loop interferometer for simultaneous measurement of directional torsion and temperature," Appl. Opt. **59**(36), 11325–11331 (2020).
- 33. Q. Zhou, W. G. Zhang, L. Chen, *et al.*, "Fiber torsion sensor based on a twist taper in polarization-maintaining fiber," Opt. Express **23**(18), 23877–23886 (2015).
- 34. Y. Q. Zhu, Y. S. Yu, Y. Zhao, *et al.*, "Highly sensitive directional torsion sensor based on a helical panda fiber taper," IEEE Photon. Technol. Lett. **31**(13), 1009–1012 (2019).
- S. J. Duan, X. Y. Bai, X. Y. Kang, et al., "High sensitive torsion sensor based on cascaded pre-twisted taper and multi-mode fiber sheets," IEEE Photon. Technol. Lett. 31(19), 1588–1591 (2019).
- Y. Y. Xu, H. F. Lin, and A. Zhou, "A pre-twisted taper in dual-side hole fiber for torsion measurement with high sensitivity," IEEE Sensors J. 20(14), 7761–7765 (2020).
- 37. Q. Guo, Y. Q. Zhu, T. Q. Shan, *et al.*, "Intensity-modulated directional torsion sensor based on a helical fiber taper," Opt. Mater. Express 11(1), 80–88 (2021).
- 38. N. Kishi and E. Yamashita, "A simple coupled-mode analysis method for multiple-core optical fiber and coupled dielectric waveguide structures," IEEE Trans. Microwave Theory Techn. 36(12), 1861–1868 (1988).
- 39. A. W. Snyder, "Coupled-mode theory for optical fibers," J. Opt. Soc. Am. 62(11), 1267-1277 (1972).
- Y. Murakami and S. Sudo, "Coupling characteristics measurements between curved waveguides using a two-core fiber coupler," Appl. Opt. 20(3), 417–422 (1981).
- X. Q. Ma, C. H. Liu, G. Q. Chang, et al., "Angular-momentum optical waves in chirally-coupled-core fibers," Opt. Express 19(27), 26515–26528 (2011).
- 42. P. S. J. Russell, R. Beravat, and G. K. L. Wong, "Helically twisted photonic cryatal fibers," Phil. Trans. R. Soc. A. 375(2087), 20150440 (2017).
- C. Liu, Y. J. Jiang, B. B. Du, et al., "Strain-insensitive twist and temperature sensor based on seven-core fiber," Sensors and Actuators A: Physical 290, 172–176 (2019).
- 44. Y. J. Li, P. Lu, Z. Y. Qu, et al., "An optical fiber twist sensor with temperature compensation mechanism based on T-SMS structure." IEEE Photonics J. 12(6), 1–8 (2020).
- F. Zhang, R. H. Xu, J. P. Wei, et al., "In-line Mach-Zehnder interferometer for simultaneous measurement of temperature and directional torsion," Optik 226(1), 165497 (2021).
- 46. X. H. Fu, Y. P. Zhang, Y. F. Wang, *et al.*, "A temperature sensor based on tapered few mode fiber long-period grating induced by CO₂ laser and fusion tapering," Opt. Laser Technol. **121**, 105825 (2020).
- 47. Y. X. Zhang, A. Zhou, B. Y. Qin, et al., "Refractive index sensing characteristics of single-mode fiber-based modal interferometers," J. Lightwave Technol. 32(9), 1734–1740 (2014).
- 48. A. M. Vengsarkar, W. C. Michie, L. Jankovic, *et al.*, "Fiber-optic dual-technique sensor for simultaneous measurement of strain and temperature," J. Lightwave Technol. **12**(1), 170–177 (1994).
- W. Jin, W. C. Michie, G. Thursby, et al., "Simultaneous measurement of strain and temperature: Error analysis," Opt. Eng 36(2), 598–609 (1997).